analytical chemistry

pubs.acs.org/ac Article

Potential- and Color-Resolved Electrochemiluminescence of Polymer Dots for Array Imaging of Multiplex MicroRNAs

Ningning Wang, Lizhen Chen, Weiwei Chen, and Huangxian Ju*

Cite This: *Anal. Chem.* 2021, 93, 5327−5333 Read Online

ACCESS | Metrics & More | Article Recommendations | Supporting Information

ABSTRACT: The development of electrochemiluminescence (ECL) emitters remains a great research interest in ECL analysis. Herein, luminol-doped polymer dots (L-Pdots) and diethylamine-coupled Pdots (N-Pdots) were synthesized to design a both potential- and color-resolved ECL strategy. L-Pdots showed the maximum ECL emission at 450 nm in the presence of hydrogen peroxide at +0.6 V, while the maximum emission of N-Pdots was at 675 nm under +1.0 V. This strategy was conveniently used to construct a novel ECL array imaging method for high-throughput detection of two microRNAs (miRNAs). The array was prepared with the mixture of L-Pdots and N-Pdots that were covalently modified with quencher-labeled DNAs, respectively, to recognize the corresponding miRNAs. Upon the addition of duplex-specific nuclease, the DNAs hybridized with miRNAs were digested to release the quenchers and miRNAs, which led to the ECL recovery of Pdots and target-cyclic signal amplification. By imaging the array at +0.6 and +1.0 V and using miRNA-21 and miRNA-205 as the analytes, the blue and red channel images could be extracted to quantify these miRNAs with detection limits of 2.5 and 3.1 pM, respectively. This work provides a new family member of potential- or color-resolved ECL emitters and successfully realizes the simultaneous and high-throughput sensing of multiplex miRNAs.

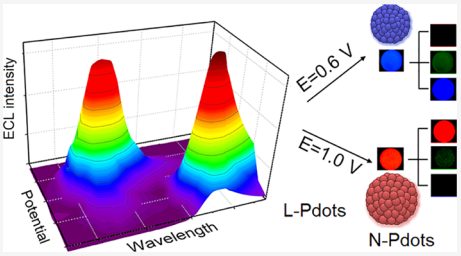

INTRODUCTION

Electrochemiluminescence (ECL) as a proven technique has been widely used in commercial immunoassays for clinical diagnosis because of its low background, high sensitivity, wide detection range, and simple instrumentation.[1−3] The simultaneous measurement of multiple biomarkers is always a hot research topic in the ECL biosensing field for early screening and evaluating the extent of disease as well as monitoring cancer therapy[4−6] because the occurrence and development of a disease are usually accompanied by the abnormality of multiple markers.[7] The potential-resolved ECL system is a vital part for high-throughput detection. Various ruthenium(II)/iridium(III) complex-,[8−10] semiconductor nanocrystal-,[11,12] quantum dot-,[13,14] or carbon nitride nanosheet-[15,16] induced potential-resolved ECL systems have been developed because of their high ECL efficiency or diversified ECL behaviors. However, this system is limited by a narrow choice of ECL luminophores. Sometimes, the water-insoluble or toxic characteristics of ECL emitters seem to restrict their application in biological sample analysis. Besides, intensity-based potential-resolved ECL analysis usually contains an inevitable error because each emitter can persistently generate ECL as long as the electrode potential exceeds the corresponding threshold value. Thus, Su and co-workers coupled spectrometers to avoid the influence of the threshold value for potential-resolved ECL multiplex immunoassay.[17] Searching for applicable ECL emitters and detection modes to enable multiplexed detection with good water-dispersity, sufficient modification sites, negligible cytotoxicity, and affordable devices still remains a current research interest.

Polymer dots (Pdots) prepared by nanoprecipitation have acted as a kind of novel ECL emitter for detection of a wide range of analytes, such as proteins,[18] microRNAs (miRNAs),[19,20] small moleculars,[21,22] and cells[23] owing to the high brightness, good biocompatibility, and tunable luminescent features. The ECL wavelength and potential of Pdots can be adjusted continuously, thanks to the tunable optical and electrical properties, by introducing intramolecular electron transfer,[23] donor−acceptor type, or electroactive monomer.[24,25] More importantly, Pdots can also be simply and effectively modified by physically incorporating small molecule dyes that are insoluble in water into functional polymers.[26] Therefore, developing Pdot-based potential-resolved ECL by coupling color or wavelength resolution is an effective and viable approach to broaden the potential-resolved ECL family.

In this work, a Pdot-based potential- and color-resolved ECL system was designed in which luminol was encapsulated into poly(styrene-*co*-maleic anhydride) (PSMA) to prepare L-Pdots and act as the low-potential emitter, and diethylamine was

Received: February 9, 2021
Accepted: March 9, 2021
Published: March 17, 2021

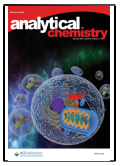

https://doi.org/10.1021/acs.analchem.1c00620
Anal. Chem. 2021, 93, 5327−5333

Scheme 1. Schematic Diagrams of (A) Preparation of Probe 21 and Probe 205 and (B) ECL Imaging Array for Analysis of miRNA-21 and miRNA-205.

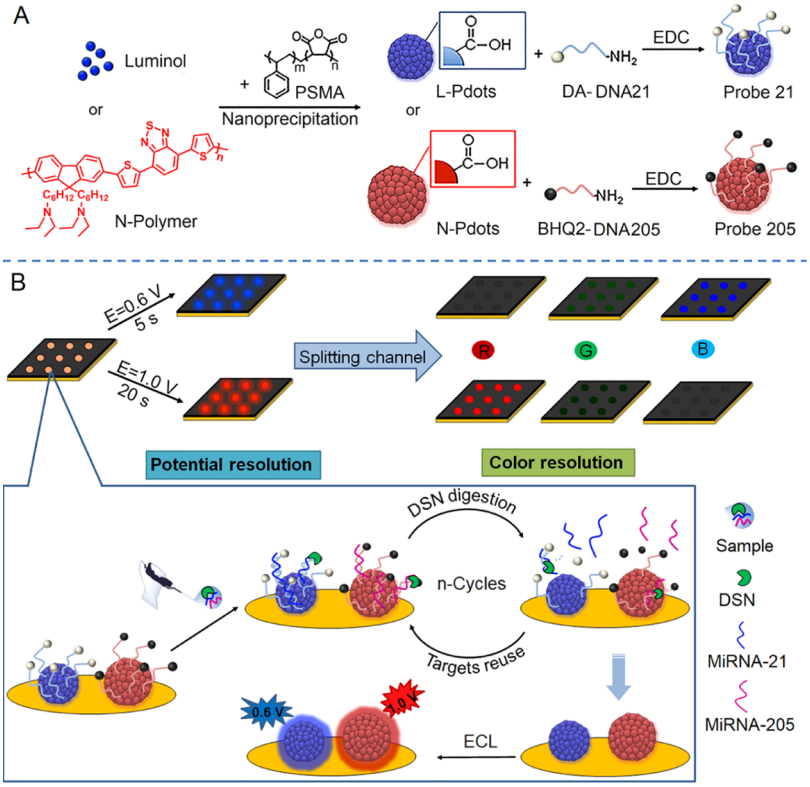

coupled with poly[2,7-(9,9-dioctylfluorene)-*alt*-4,7-bis-(thiophen-2-yl)benzo-2,1,3-thiadiazole] to prepare coreactant-embedded N-Pdots through nanoprecipitation and act as a high-potential emitter. Moreover, L-Pdots emitted the blue ECL in the presence of an H_2O_2 coreactant, while N-Pdots could emit the self-enhanced red ECL in PBS due to the dual intramolecular electron transfer. By splitting the true-color photograph of ECL imaging for Pdots into red, green, and blue (RGB) channels, L-Pdots consisted of strong blue light, weak green light, and negligible red light, while N-Pdots consisted of negligible blue light, weak green light, and strong red light. Therefore, the blue channel intensity of L-Pdots at a low potential and the red channel intensity of N-Pdots at a high potential did not interfere with each other, which avoided the influence of thresholds in a simultaneous test of multiplex analytes, leading to a new resolved strategy.

miRNAs play crucial roles in post-transcriptional regulation of gene expression, which act as promising biomarkers for cancer diagnosis.[27] Simultaneous detection of multiple miRNAs has a potential role in the classification and diagnosis of diseases.[28] Here, we used L-Pdots and N-Pdots as biocompatible ECL emitters to immobilize DA-DNA21 (probe 21) and BHQ2-DNA205 (probe 205) for design of a target-cyclic signal amplification with duplex-specific nuclease (DSN), respectively, where DA and BHQ2 are the ECL quenchers, dopamine and black hole quencher 2, of L-Pdots and N-Pdots, and DNA21 and DNA205 are used to hybridize miRNA-21 and miRNA-205 in the sample solution, respectively. Upon the recognition of miRNA-21 and miRNA-205 to probe 21 and probe 205, the strong ECL emission of L-Pdots and N-Pdots was recovered due to the release of quenchers in the presence of DSN, respectively, which amplified the "off−on" signal to achieve the potential- and color-resolved ECL imaging of miRNA-21 and miRNA-205. The designed ECL array imaging method could differentiate cell subtypes of non-small-cell lung cancer by simultaneously sensing miRNA-21 and miRNA-205 in cell lysate, indicating its promising application in clinical diagnosis and disease prognosis.

EXPERIMENTAL SECTION

Materials, Reagents, and Apparatus. The detailed information is listed in the Supporting Information.

Preparation of L-Pdots and N-Pdots. L-Pdots and N-Pdots were prepared by nanoprecipitation,[29] which was performed by ultrasonically degassing the mixture of 200 μg mL^{-1} luminol and 100 μg mL^{-1} PSMA and the mixture of 200 μg mL^{-1} N-Polymer (Supporting Information) and 40 μg mL^{-1} PSMA in 2 mL of THF for 20 min and then injecting the mixtures into 8 mL of water with ultrasonic treatment for another 3 min, respectively (Scheme 1A). Here, PSMA acted as carboxyl-functionalized copolymer to provide carboxyl groups.[30] After removing the THF by gentle rotary evaporation and filtrating through a 0.22 μm poly(ether sulfones) syringe filter, 100 μg mL^{-1} L-Pdot and N-Pdot dispersions were obtained.

Preparation of Probe 21 and Probe 205. DA-DNA21 was first prepared by mixing dopamine hydrochloride (2 mM, 5 μL) and sulfo-SMCC (2 mM, 5 μL) at room temperature for 6 h, and then HS-DNA21-NH_2 (100 μM, 100 μL) whose disulfide bonds have been reduced with TCEP (100 mM, 10 μL) for 2 h, followed by L-Pdots (100 μg mL^{-1}, 1 mL), *N*-(2-hydroxyethyl)piperazine-*N*′-ethanesulfonic acid (1 M, 20 μL) and poly(ethylene glycol) (5% w/v, 20 μL) to adjust the pH to

https://doi.org/10.1021/acs.analchem.1c00620
Anal. Chem. 2021, 93, 5327−5333

7.1. The obtained DA-DNA21 (40 μL) was added in EDC (10 mg mL^{-1}, 100 μL) with gentle vibration for 4 h at room temperature to get the probe 21 dispersion (Scheme 1A), which was stored at 4 °C in dark for further use. Similarly, probe 205 was prepared by replacing DA-DNA21 and L-Pdots with BHQ2-DNA205 and N-Pdots, respectively.

Preparation of an ECL Imaging Array. The ECL array was first prepared by pasting a porous sticker on Au-coated ITO (Au/ITO) as the electrode substrate, which was fabricated by electron beam evaporation with 5 nm chrome and 50 nm gold. The mixture of 25 μg mL^{-1} probe 21 and probe 205 was then dropped into the holes of the array (2 μL/well) to dry at 37 °C for 30 min, followed by washing thrice with 0.1 M PBS (pH 7.4) to remove free DNA and unreacted reagents for getting the ECL imaging array (Scheme S2).

ECL Imaging Detection. After 2 μL of a mixture of DSN (0.2 U) and miRNAs or sample was added into each well to incubate for 40 min at 50 °C, the resulting array was washed row by row three times by gently dropping a washing buffer (10 mM PBS, pH 7.4) to avoid the cross-contamination to remove the released quenchers (Scheme 1B), which was dried at 37 °C for 20 min to apply a constant potential of +0.6 V for 5 s and +1.0 V for 20 s in 0.1 M pH 7.4 PBS containing 20 mM H_2O_2 to get two images, respectively, in a self-made ECL imaging system.[4] Adobe photoshop software was used to obtain the blue value of the image captured at +0.6 V and the red value of the image captured at +1.0 V for quantifying the concentration of miRNA-21 and miRNA-205.

RESULTS AND DISCUSSION

Characterization of L-Pdots and N-Pdots. The successful synthesis and characterization of the N-polymer are shown in Scheme S1 and Figure S1. The atomic force microscopy (AFM) images of L-Pdots and N-Pdots showed the spherical and monodisperse feature with a height distribution of 10−12 and 21−23 nm, respectively (Figure 1A,B). The X-ray photoelectron spectroscopy (XPS) analysis of N-Pdots revealed the existence of quaternary ammonium at 401.6 eV compared with L-Pdots, which showed only a peak of N 1s for luminol at 398.5 eV (Figure 1C). Considering the overlap between the absorption spectrum of N-Pdots and the emission spectrum of L-Pdots (Figure S2), the fluorescence resonance energy transfer (FRET) between N-Pdots and L-Pdots should be first excluded for subsequent detection. The FL emission of N-Pdots at 672 nm remanded consistent for the mixture of N-Pdots with different concentrations of L-Pdots at the exciting wavelength of 375 nm (Figure 1D), indicating the absence of FRET.

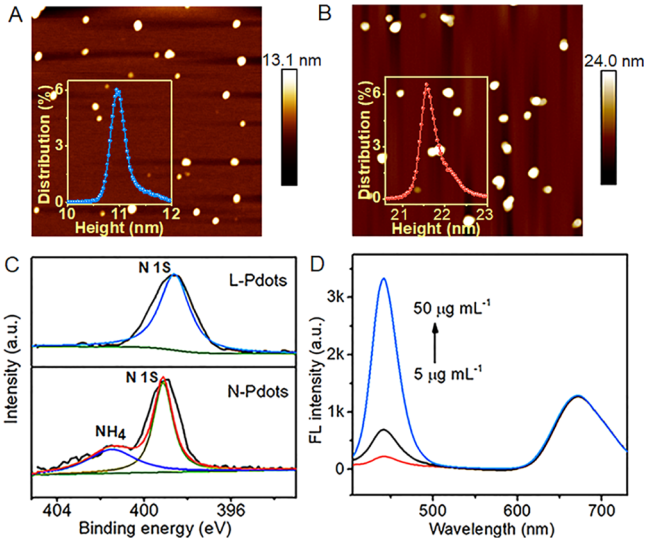

Figure 1. AFM images and particle height distribution of (A) L-Pdots and (B) N-Pdots. (C) N 1s and NH_4 XPS spectra of L-Pdots and N-Pdots. (D) FL spectra of 50 μg mL^{-1} N-Pdots mixed with 5, 10, 50 μg mL^{-1} L-Pdots (λ_{ex} = 375 nm).

ECL Mechanism. The electrochemical and ECL behaviors of L-Pdots and N-Pdots were studied by modifying them on Au/ITO. As shown in Figure 2A, the oxidation peak of L-Pdots

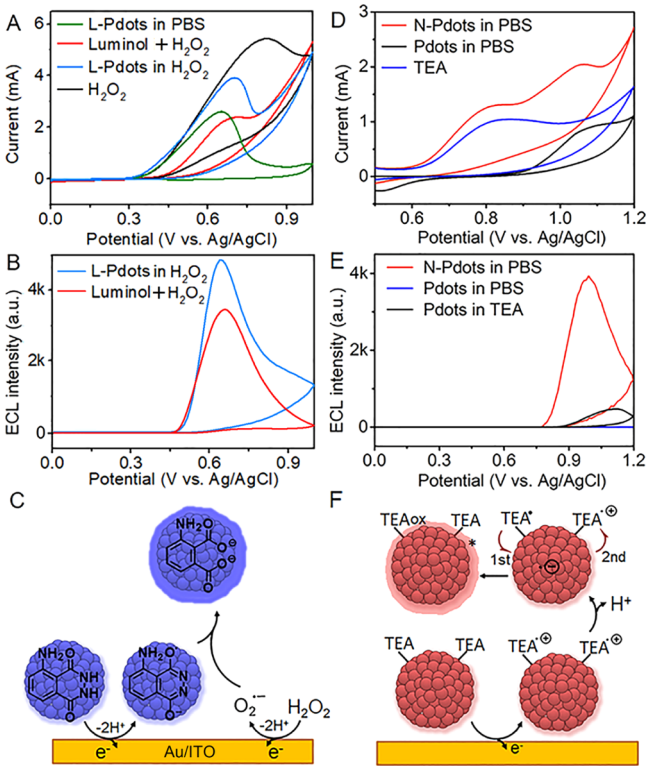

Figure 2. (A) CV curves of L-Pdot-modified Au/ITO in 0.1 M pH 7.4 PBS (green) and PBS + 25 mM H_2O_2 (blue) and bare Au/ITO in 25 mM H_2O_2 (black) and 100 μg mL^{-1} luminol +1 25 mM H_2O_2 solution (red). (B) ECL curves of L-Pdot-modified Au/ITO in 0.1 M PBS + 25 mM H_2O_2 (blue) and bare Au/ITO in100 μg mL^{-1} luminol + 25 mM H_2O_2 solution (red). (C) ECL mechanism of L-Pdots in H_2O_2. (D) CV curves of Pdot-modified Au/ITO (black) in 0.1 M PBS and bare Au/ITO in 0.1 M PBS containing N-Pdots (red) or 25 mM TEA (blue). (E) ECL curves of N-Pdot- (red) and Pdot- (blue)modified Au/ITO in 0.1 M PBS, and Pdot-modified Au/ITO in 0.1 M PBS containing 10 mM TEA (black). (F) ECL mechanism of intramolecular electron transfer for N-Pdots in PBS.

in H_2O_2 (blue curve) occurred at the same value of +0.7 V as that of the luminol and H_2O_2 system (red curve), which demonstrated the same electrochemical oxidation of L-Pdots under the assistance of H_2O_2. Their ECL occurred after +0.5 V and tended to maximum emission at around +0.7 V (Figure 2B), which resulted from the excited intermediates produced by the oxidation product of luminol and O2•−.[31] The detailed ECL mechanism is described in Figure 2C, which was consistent with the classical luminol and H_2O_2 system.[32] N-Pdots showed two peaks at +0.8 and +1.0 V (Figure 2D, red

https://doi.org/10.1021/acs.analchem.1c00620
Anal. Chem. 2021, 93, 5327−5333

curve). The first peak was attributed to the oxidation of tertiary amine groups similar to TEA (Figure 2D, blue curve), and the second peak resulted from the oxidation of Pdots (Figure 2D, black curve), which was prepared by nanoprecipitation of PSMA and the polymer without tertiary amine groups (PFO-DBT). According to the onset potential of ECL for N-Pdots (Figure 2E, red curve), which was earlier than the oxidation of Pdots (Figure 2D, black curve), ECL was excited by the oxidation of tertiary amine groups followed with two-step intramolecular electron transfer (Figure 2F).[23]

Potential- and Color-Resolved ECL. The ECL curves of L-Pdot-modified Au/ITO showed an emission peak at +0.6 V with the onset potential of +0.4 V in 25 mM H_2O_2 (Figure 3A,

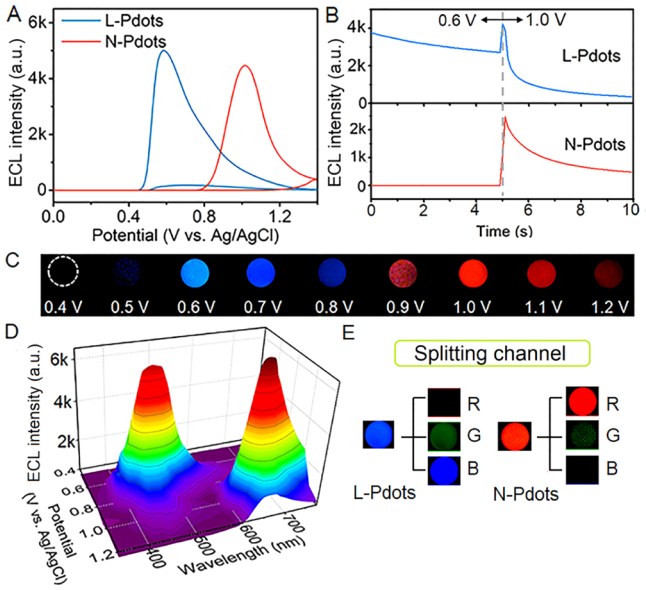

Figure 3. (A) ECL curves of L-Pdot- and N-Pdot-modified Au/ITO electrodes in 0.1 M PBS containing 25 mM H_2O_2. (B) Stepping pulse curves of L-Pdot- and N-Pdot-modified Au/ITO electrodes applying 0.6 and 1.0 V for 5 s, respectively. (C) ECL images and (D) 3D-ECL-emission spectrum of Au/ITO electrodes modified with the mixture of 10 μg mL^{-1} L-Pdots and 50 μg mL^{-1} N-Pdots at 0.4−1.2 V in 0.1 M PBS containing 25 mM H_2O_2. (E) Images of RGB channels splitting form the ECL images of L-Pdot-modified Au/ITO at 0.6 V for 5 s in 0.1 M PBS containing 25 mM H_2O_2 and N-Pdot-modified Au/ITO at 1.0 V for 20 s in 0.1 M PBS.

blue curve), while N-Pdot-modified Au/ITO exhibited the maximum emission at +1.0 V with the onset potential of +0.7 V in PBS (Figure 3A, red curve). Stepping pulse scanning was employed to investigate the potential-resolved ECL behaviors. As shown in Figure 3B, at the initial stepping potential of +0.6 V, strong ECL emission of L-Pdots was observed but not in N-Pdots. As the second stepping potential reached +1.0 V, the ECL of L-Pdots first showed an enhancement process and then decayed, while that of N-Pdots increased and then decreased gradually. This phenomenon indicated that in the mixture of L-Pdots and N-Pdots, ECL only came from L-Pdots at +0.6 V, while ECL emission at +1.0 V could be attributed to both L-Pdots and N-Pdots. Thus, the intensity-based potential-resolved ECL could not separate the detection signals of the two components, and the introduction of color-resolved ECL imaging can effectively eliminate the effect of L-Pdots on the ECL signal at +1.0 V.

As the proof-of-concept, L-Pdots were mixed with N-Pdots to examine the potential- and color-resolved ECL emission. The true-color ECL images captured at different potentials of the mixture exhibited the changes of both color and intensity (Figure 3C). By collecting the corresponding spectra, two distinguishable ECL spectral domains were observed (Figure 3D). In a low potential range, the whole spectra were dominated by L-Pdots with a maximum emission at 425 nm under +0.6 V, while a peak at 673 nm at a high potential mainly resulted from N-Pdots, which could be better distinguished in the top view of 3D-ECL-emission spectra (Figure S3). The top view clearly illustrated that the ECL generated at +0.6 V totally resulted from L-Pdots, while the ECL emission at +1.0 V mainly was contributed by N-Pdots.

Furthermore, the ECL emission of L-Pdots consisted of strong blue light, weak green light, as well as negligible red light, but N-Pdots consisted of negligible blue light, weak green light, and strong red light, which were observed by splitting the true-color ECL images into RGB channels (Figures 3E and S4). Thus, the blue channel of the image taken at +0.6 V was only generated by L-Pdots, while the red channel of the image captured at +1.0 V was only attributed by N-Pdots, and the contribution of L-Pdots to total ECL intensity at +1.0 V could be eliminated, which provided a basis for the quantitative detection of the mixture.

Characterization of Probe 21 and Probe 205. The successful conjugation of DA and sulfo-SMCC was demonstrated by MALDI-MS (Figure S5). After the L-Pdots were functionalized with DA-DNA21, probe 21 showed three absorption peaks at 279, 310, and 350 nm (Figure S6A). The absorption peak at 279 nm was coincident with DA, while the absorption peaks at 310 and 350 nm were coincident with L-Pdots. Besides, the stronger absorbance intensity of probe 21 at 260 nm than that of L-Pdots also indicated the successful conjugation of DA-DNA21 on the Pdot surface. Similarly, probe 205 showed three absorption peaks at 260, 387, and 595 nm (Figure S6B). The absorption peak at 287 nm was consistent with N-Pdots, and the red-shifted absorption peak at 595 nm resulted from the introduction of BHQ2. The significantly enhanced absorption peak at 260 nm could imply the conjugation of BHQ2-DNA205 on N-Pdots. The conjugation of DA-DNA21 and BHQ2-DNA205 also led to a negative increase of Zeta-potential from −26.4 mV of L-Pdots to −45.6 mV of probe 21 and +18.7 mV of N-Pdots to −6.7 mV of probe 205 (Figure S7).

The quenching effect was evaluated by comparing L-Pdots with probe 21 and N-Pdots with probe 205, respectively. The conjugation of DA to L-Pdots led to a quenching of 93.4% emission (Figure S8A), which could be attributed to the fact that the oxidization of DA consumed notable amounts of ROSs, resulting in the remarkable decrease of the ECL signal of luminol.[33] BHQ2 could quench 89.3% ECL of N-Pdots (Figure S8B) due to its wide absorption range. Thus, the self-quenched probes 21 and 205 were prepared for subsequent detection owing to their low background.

Characterization of Imaging Array. Electrochemical impedance spectroscopy (EIS) measurements were performed to characterize the construction of the imaging array (Figure 4A). Compared with bare Au/ITO (curve a), the probes 21- and 205-coated Au/ITO exhibited significantly increased electron-transfer resistance R_{et} (curve b). After the imaging array was incubated with target miRNAs and DSN, miRNAs hybridize respectively with the DNA strands on the probes to

https://doi.org/10.1021/acs.analchem.1c00620
Anal. Chem. 2021, 93, 5327−5333

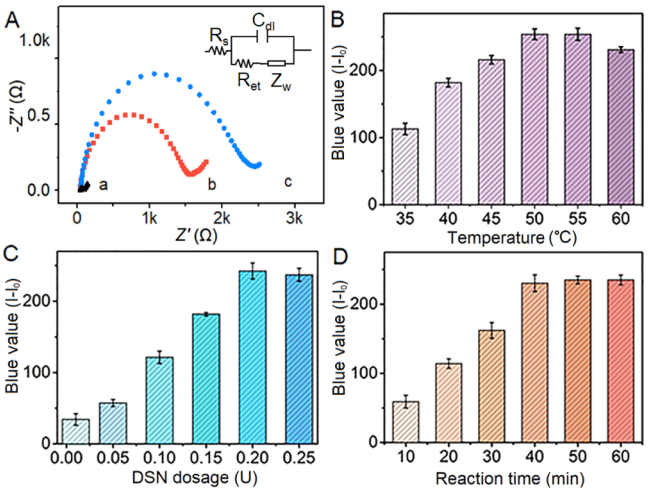

Figure 4. (A) EIS of Au/ITO (a), probe 21-modified Au/ITO and (b) after incubation with 1 nM miRNA-21 and 0.2 U DSN (c). Effects of (B) temperature, (C) DSN dosage in each hole and (D) incubation time on ECL imaging signal for miRNA-21 at 1 nM (n = 3).

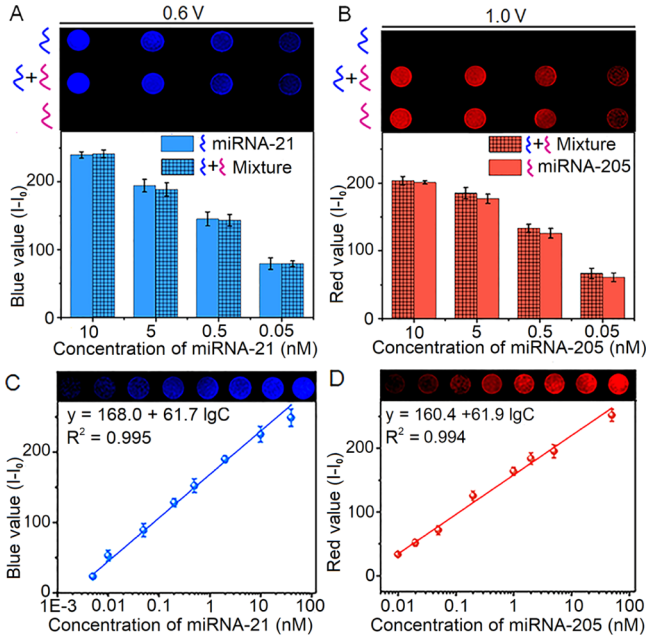

Figure 5. ECL images and intensity from (A) blue and (B) red channels for detection of 10, 5, 0.5, and 0.05 nM miRNA-21, miRNA-205, and their mixture of equivalent concentration, respectively. ECL images and calibration curves for detection of (C) miRNA-21 and (D) miRNA-205 (n = 3).

form a double-stranded complex, which were digested by DSN to release the quenchers and target miRNAs[34] (Figure S9); thus, the R_{et} decreased (curve c). These results proved the feasibility of a target-initiated cycle for "off−on" signal amplification.

Optimization of Detection Conditions. Considering that the melting temperatures of the miRNA-21 and 205 were 59.4 and 63.8 °C (Figure S10), respectively, the incubation temperature was first optimized in the presence of 1 nM miRNA-21. The blue value of ECL images from L-Pdots tended to the maximum at 50 °C, which was chosen for the subsequent experiments (Figure 4B).

The amount of DSN was an important factor affecting the detection performance. As shown in Figure 4C, the blue value of ECL images increased with the increasing enzyme dosage and reached the plateau value at 0.2 U DSN, which was selected as the optimal amount. Besides, the incubation time determined the digestion reaction degree and the amount of released quenchers. The blue value of ECL images for L-Pdots increased with the extension of the reaction time and tended to the constant value at 40 min (Figure 4D), which was selected as the optimum time for the reaction.

Performance of ECL Array Imaging. In order to explore the reliability of the designed ECL imaging array for simultaneous detection of two miRNAs, the results of simultaneous detection and separate detection of miNRA-21 and miRNA-205 at different concentrations were compared. As shown in Figure 5A,B, only miRNA-21 were added in the first row of the imaging array as well as only miNRA-205 in the third row, and the mixtures of the two miRNAs with equal concentrations were added in the second row. The blue value of the image at +0.6 V represented the concentration of miRNA-21, and the detection results of the mixture were consistent with those of pure miRNA-21 (Figure 5A). Similarly, the red value of the image at +1.0 V indicated the concentration of miRNA-205, and no difference between the detection results of miRNA-205 in the mixture and pure miRNA-205 solution was observed (Figure 5B).

Under optimal conditions, the ECL array imaging was used for simultaneously detecting miRNA-21 and miRNA-205, which were quantified by the blue and red values from the ECL images captured at +0.6 and +1.0 V, respectively. The blue or red value increased with the increasing target concentration, and the plots of their integration from the marked area versus the logarithm of miRNA concentration showed good linearity in the concentration range of 5 pM to 40 nM and 10 pM to 50 nM with the correlation coefficients of 0.996 and 0.994 for miRNA-21 and miRNA-205, respectively (Figure 5C,D). The limits of detection were 2.5 and 3.1 pM for miRNA-21 and miRNA-205, corresponding to a signal-to-noise ratio of 3, respectively.

The selectivity of this strategy was further evaluated by comparing the blue or red value of ECL images in the presence of different miRNAs, including the target miRNAs as well as their single and triple base-mismatched miRNAs (1-mis and 3-mis), miRNA-141, and miRNA-203. As expected, the array only showed the obvious response to corresponding target miRNA (Figure 6A), showing excellent specificity.

Real Sample Analysis. The practicability of the potential- and color-resolved ECL array imaging was first evaluated with total RNA extracted from non-small-cell lung cancer cells, both adenocarcinoma A549 cells and squamous cell carcinoma H520 cells. As shown in Figure 6B, A549 cells showed a high expression of miRNA-21, and H520 cells highly expressed both miRNA-21 and miRNA-205. The amount of miRNA-21 in a single A549 cell and H520 cell could be calculated as 4306 copies and 3702 copies, while the amount of miRNA-205 was 556 copies and 3496 copies, respectively. These results were in great agreement with quantitative real-time polymerase chain reaction [(q-RT-PCR), Figure S11] and kept the same trend as that in previous work,[35] indicating the reliability of the ECL array imaging of cell lysate analysis.

Recovery experiments were further applied to detect the amount of target miRNAs in human serum by spiking various concentrations of miRNA-21 and miRNA-205. As shown in

https://doi.org/10.1021/acs.analchem.1c00620
Anal. Chem. 2021, 93, 5327−5333

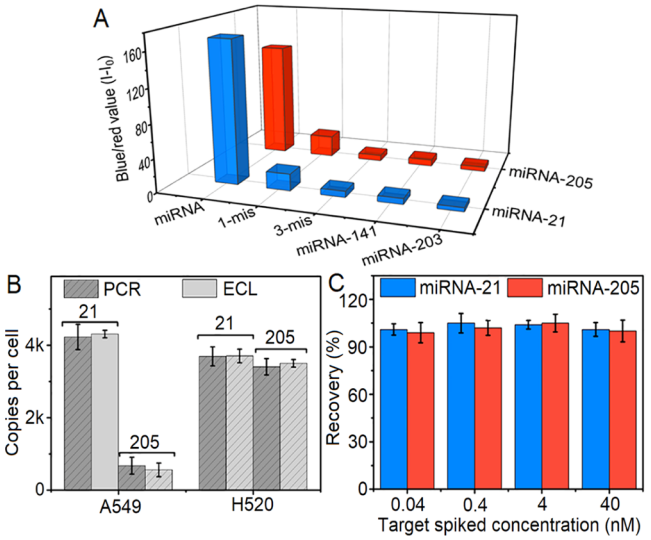

Figure 6. (A) Specificity of the proposed imaging method for detection of miRNA-21, miRNA-205, their single-base-mismatched and three-base-mismatched miRNA, miRNA-141, and miRNA-203 at 1 nM. (B) Average miRNA-21 and miRNA-205 copy number per A549 and H520 cell detected with the proposed method and q-RT-PCR (n = 3). (C) Recovery of diverse concentrations of miRNA-21 or miRNA-205 spiked in 10× diluted human serum with the proposed method and the q-RT-PCR method (n = 3).

Figure 6C, the recovery rate ranged from 95 to 105%, and the relative standard deviations were less than 10%, which were also similar with the results by q-RT-PCR, indicating the potential value of the designed imaging array in practice.

CONCLUSIONS

A potential- and color-resolved ECL array imaging method has been developed with two kinds of Pdots for simultaneous detection of two miRNAs. These Pdots can be simply synthesized with PSMA and luminol or an N-polymer (diethylamine-coupled polymer) via nanoprecipitation. L-Pdots show excellent blue ECL emission at +0.6 V in the presence of H_2O_2 as the coreactant, which does not affect the red ECL emission of N-Pdots at +1.0 V in PBS. Compared to traditional potential-resolved ECL system, the interference of threshold produced by the low potential emitter at high potentials can be avoided. By covalently binding quencher-labeled DNAs specific to miRNA-21 and miRNA-205 with these Pdots, two specific probes have been proposed for preparation of the ECL imaging array, which can achieve the target-initiated cycle for "off−on" signal amplification in the presence of targets and DSN. By extracting the intensity values of ECL images in the blue and red channels, miRNA-21 and miRNA-205 have been quantified respectively, which shows high sensitivity, good selectivity, excellent accuracy and acceptable precision towards cell lysates and spiked miRNAs in human serum samples. The results demonstrate great potential of the proposed potential- and color-resolved ECL strategy, the ECL imaging array and the simultaneous detection method in cancer clinical diagnosis and prognosis.

ASSOCIATED CONTENT

Supporting Information

The Supporting Information is available free of charge at https://pubs.acs.org/doi/10.1021/acs.analchem.1c00620.

Extraction of miRNAs from cell lysate, q-RT-PCR and gel electrophoresis analysis, oligonucleotide sequences, synthetic route of N-Polymer, construction of ECL imaging array, ^{1}H NMR for N-Polymer, UV−vis spectrum of N-Pdots and FL spectrum of L-Pdots, top view of 3D-ECL-emission spectra for the mixture of L-Pdots and N-Pdots, splitting RGB channels of L-Pdots and N-Pdots, MALDI-MS spectrum of Mal-dopamine, UV−vis spectra, zeta-potential and ECL curves of probes, polyacrylamide gel electrophoresis image, as well as UV melting and q-RT-PCR calibration curves of miRNAs (PDF).

AUTHOR INFORMATION

Corresponding Author

Huangxian Ju − *State Key Laboratory of Analytical Chemistry for Life Science, School of Chemistry and Chemical Engineering, Nanjing University, Nanjing 210023, P. R. China;* orcid.org/0000-0002-6741-5302; Phone: +86-25-89683593; Email: hxju@nju.edu.cn; Fax: +86-25-89683593

Authors

Ningning Wang − *State Key Laboratory of Analytical Chemistry for Life Science, School of Chemistry and Chemical Engineering, Nanjing University, Nanjing 210023, P. R. China*

Lizhen Chen − *State Key Laboratory of Analytical Chemistry for Life Science, School of Chemistry and Chemical Engineering, Nanjing University, Nanjing 210023, P. R. China*

Weiwei Chen − *State Key Laboratory of Analytical Chemistry for Life Science, School of Chemistry and Chemical Engineering, Nanjing University, Nanjing 210023, P. R. China*

Complete contact information is available at: https://pubs.acs.org/10.1021/acs.analchem.1c00620

Notes

The authors declare no competing financial interest.

ACKNOWLEDGMENTS

We acknowledge the financial support of the National Natural Science Foundation of China (22004068, 21827812, 21890741, 21635005).

REFERENCES

(1) Zanut, A.; Palomba, F.; Scota, M. R.; Rebeccani, S.; Marcaccio, M.; Genovese, D.; Rampazzo, E.; Valenti, G.; Paolucci, F.; Prodi, L. *Angew. Chem., Int. Ed.* **2020**, *59*, 21858−21863.

(2) Zhao, M.-L.; Zeng, W.-J.; Chai, Y.-Q.; Yuan, R.; Zhuo, Y. *Anal. Chem.* **2020**, *92*, 11044−11052.

(3) Meso Scale Diagnostics. www.mesoscale.com.web (accessed January 12, 2021).

(4) Wang, N.; Feng, Y.; Wang, Y.; Ju, H.; Yan, F. *Anal. Chem.* **2018**, *90*, 7708−7714.

(5) Deiss, F.; LaFratta, C. N.; Symer, M.; Blicharz, T. M.; Sojic, N.; Walt, D. R. *J. Am. Chem. Soc.* **2009**, *131*, 6088−6089.

(6) Wang, Y.-Z.; Ji, S.-Y.; Xu, H.-Y.; Zhao, W.; Xu, J.-J.; Chen, H.-Y. *Anal. Chem.* **2018**, *90*, 3570−3575.

(7) Ma, Z.; Liu, N. *Expert Rev. Mol. Diagn.* **2015**, *15*, 1075−1083.

(8) Doeven, E. H.; Barbante, G. J.; Hogan, C. F.; Francis, P. S. *ChemPlusChem* **2015**, *80*, 456−470.

(9) Doeven, E. H.; Zammit, E. M.; Barbante, G. J.; Hogan, C. F.; Barnett, N. W.; Francis, P. S. *Angew. Chem., Int. Ed.* **2012**, *51*, 4354−4357.
(10) Doeven, E. H.; Zammit, E. M.; Barbante, G. J.; Francis, P. S.; Barnett, N. W.; Hogan, C. F. *Chem. Sci.* **2013**, *4*, 977−982.
(11) Hesari, M.; Swanick, K. N.; Lu, J.-S.; Whyte, R.; Wang, S.; Ding, Z. *J. Am. Chem. Soc.* **2015**, *137*, 11266−11269.
(12) He, Y.; Hou, S.; Yang, L.; Zhang, F.; Zou, G. *Chem. —Eur. J.* **2018**, *24*, 9592−9597.
(13) Du, D.; Shu, J.; Guo, M.; Haghighatbin, M. A.; Yang, D.; Bian, Z.; Cui, H. *Anal. Chem.* **2020**, *92*, 14113−14121.
(14) Wang, X.; Liu, H.; Qi, H.; Gao, Q.; Zhang, C. *J. Mater. Chem. B* **2020**, *8*, 3598−3605.
(15) Wang, J.; Haghighatbin, M. A.; Shen, W.; Mi, L.; Cui, H. *Anal. Chem.* **2020**, *92*, 7062−7070.
(16) Jin, Y.; Kang, Q.; Guo, X.; Zhang, B.; Shen, D.; Zou, G. *Anal. Chem.* **2018**, *90*, 12930−12936.
(17) Guo, W.; Ding, H.; Gu, C.; Liu, Y.; Jiang, X.; Su, B.; Shao, Y. *J. Am. Chem. Soc.* **2018**, *140*, 15904−15915.
(18) Fang, D.; Zhang, S.; Dai, H.; Lin, Y. *Biosens. Bioelectron.* **2019**, *146*, 111768.
(19) Luo, J.-H.; Li, Q.; Chen, S.-H.; Yuan, R. *ACS Appl. Mater. Interfaces* **2019**, *11*, 27363−27370.
(20) Liu, D.; Zhang, X.; Zhao, J.; Chen, S.; Yuan, R. *Biosens. Bioelectron.* **2020**, *150*, 111872.
(21) Wang, Z.; Pan, J.; Li, Q.; Zhou, Y.; Yang, S.; Xu, J. J.; Hua, D. *Adv. Funct. Mater.* **2020**, *30*, 2000220.
(22) Chen, H.; Zhang, H.; Yuan, R.; Chen, S. *Anal. Chem.* **2017**, *89*, 2823−2829.
(23) Wang, N.; Gao, H.; Li, Y.; Li, G.; Chen, W.; Jin, Z.; Lei, J.; Wei, Q.; Ju, H. *Angew. Chem., Int. Ed.* **2021**, *60*, 197−201.
(24) Omer, K. M.; Ku, S.-Y.; Cheng, J.-Z.; Chou, S.-H.; Wong, K.-T.; Bard, A. J. *J. Am. Chem. Soc.* **2011**, *133*, 5492−5499.
(25) Wang, Z.; Feng, Y.; Wang, N.; Cheng, Y.; Quan, Y.; Ju, H. *J. Phys. Chem. Lett.* **2018**, *9*, 5296−5302.
(26) Feng, Y.; Sun, F.; Wang, N.; Lei, J.; Ju, H. *Anal. Chem.* **2017**, *89*, 7659−7666.
(27) Bartel, D. P. *Cell* **2009**, *136*, 215−233.
(28) Lu, Y.; Zhao, X.; Liu, Q.; Li, C.; Graves-Deal, R.; Cao, Z.; Singh, B.; Franklin, J. L.; Wang, J.; Hu, H.; Wei, T.; Yang, M.; Yeatman, T. J.; Lee, E.; Saito-Diaz, K.; Hinger, S.; Patton, J. G.; Chung, C. H.; Emmrich, S.; Klusmann, J.-H.; Fan, D.; Coffey, R. J. *Nat. Med.* **2017**, *23*, 1331−1341.
(29) Kuo, C.-T.; Thompson, A. M.; Gallina, M. E.; Ye, F. M.; Johnson, E. S.; Sun, W.; Zhao, M. X.; Yu, J. B.; Wu, I.-C.; Fujimoto, B.; DuFort, C. C.; Carlson, M. A.; Hingorani, S. R.; Paguirigan, A. L.; Radich, J. P.; Chiu, D. T. *Nat. Commun.* **2016**, *7*, 11468.
(30) Jiang, L.; Bai, H.; Liu, L.; Lv, F.; Ren, X.; Wang, S. *Angew. Chem., Int. Ed.* **2019**, *58*, 10660−10665.
(31) Gu, W.; Wang, H.; Jiao, L.; Wu, Y.; Chen, Y.; Hu, L.; Gong, J.; Du, D.; Zhu, C. *Angew. Chem., Int. Ed.* **2020**, *59*, 3534−3538.
(32) Liu, S.; Yuan, H.; Bai, H.; Zhang, P.; Lv, F.; Liu, L.; Dai, Z.; Bao, J.; Wang, S. *J. Am. Chem. Soc.* **2018**, *140*, 2284−2291.
(33) Zhang, P.; Wu, X.; Yuan, R.; Chai, Y. *Anal. Chem.* **2015**, *87*, 3202−3207.
(34) Degliangeli, F.; Kshirsagar, P.; Brunetti, V.; Pompa, P. P.; Fiammengo, R. *J. Am. Chem. Soc.* **2014**, *136*, 2264−2267.
(35) Chen, K.; Huang, Q.; Fu, T.; Ke, G.; Zhao, Z.; Zhang, X.; Tan, W. *Anal. Chem.* **2020**, *92*, 7404−7408.

https://doi.org/10.1021/acs.analchem.1c00620
Anal. Chem. 2021, 93, 5327−5333